Nanoscale

Accepted Manuscript

Nanoscale

Volume 10
Number 4
28 January 2018
Pages 1549-2172

rsc.li/nanoscale

ISSN 2040-3372

ROYAL SOCIETY
OF CHEMISTRY

PAPER
Shuping Xu, Chongyang Liang et al.
Organelle-targeting surface-enhanced Raman scattering
(SERS) nanosensors for subcellular pH sensing

NCNST

This is an Accepted Manuscript, which has been through the Royal Society of Chemistry peer review process and has been accepted for publication.

Accepted Manuscripts are published online shortly after acceptance, before technical editing, formatting and proof reading. Using this free service, authors can make their results available to the community, in citable form, before we publish the edited article. We will replace this Accepted Manuscript with the edited and formatted Advance Article as soon as it is available.

You can find more information about Accepted Manuscripts in the Information for Authors.

Please note that technical editing may introduce minor changes to the text and/or graphics, which may alter content. The journal's standard Terms & Conditions and the Ethical guidelines still apply. In no event shall the Royal Society of Chemistry be held responsible for any errors or omissions in this Accepted Manuscript or any consequences arising from the use of any information it contains.

ROYAL SOCIETY
OF CHEMISTRY

rsc.li/nanoscale

ARTICLE

Facile integration of single crystalline phthalocyanine nanowires and nanotrees as photoenhanced conductometric sensors

A. Nicolás Filippin,[a] Ángel Campos-Lendinez,[a] Juan Delgado-Alvarez,[a] Gloria Moreno-Martinez,[a] Javier Castillo-Seoane,[a] Víctor J. Rico,[a] Vanda F. Godinho,[a] Ángel Barranco,[a] Juan R. Sanchez-Valencia,[a]* Ana Borras[a]*

This article presents a reproducible and affordable methodology for fabricating organic nanowires (ONWs) and nanotrees (ONTs) light-enhanced conductometric O_2 sensors. The protocol is based on a solventless procedure for the formation of high-density arrays of nanowires and nanotrees on interdigitated electrodes. The synthesis combines physical vapour deposition for the self-assembled growth of free-phthalocyanine nanowires and soft plasma etching to prompt the nucleation sites on the as-grown OWNs to allow for the formation of nanotrees. Electrical conductivity in such low-dimensional electrodes is analysed in the context of density, length, and interconnection between nanowires and nanotrees. Further, the electrodes are immersed in water to improve the nanowires' connectivity. The response of the nanotrees as conductometric O_2 sensors is tested under different temperatures (from room temperature to 100 ºC), demonstrating that the higher surface area exposed by the nanotrees in comparison with polycrystalline thin film counterparts, effectively enhances the doping effect of oxygen and increases the response of the ONTs-based sensor. Both organic nanowires and nanotrees were applied as model systems to study the enhanced response of the sensors provided by illumination with white or monochromatic light to the organic semiconducting systems. Interestingly, the otherwise negligible sensor response at room temperature can be activated (On/Off) under LED illumination, and no dependency on the illumination wavelength for the visible range was observed. Thus, under low-power LED illumination with white light, we show a response to O_2 of 16 % and 37 % in resistivity for organic nanotrees at room temperature and 100ºC, respectively. These results open the path to developing room temperature long-lasting gas sensors based on one and three-dimensional single-crystalline small-molecule nanowires.

Introduction

The necessity for gas sensors operating at room temperature is a critical area of research, addressing the need for low-cost, low-power, portable, flexible and highly sensitive devices that could be integrated into modern electronic gadgets and wearables.[1] Traditional metal-oxide semiconductor-based sensors suffer from high operating temperatures, limiting their practical use.[2] The use of 2D materials such as graphene or MXenes for gas sensor applications has shown potential for flexible, room-temperature applications.[3] Hybrid approaches combining graphene or MXenes with more sensitive sensing materials such as metal oxides[4] or 2D transition metal dichalcogenides[5] have shown the potential to enhance sensitivity and selectivity.[3]

In this context, organic-based sensors, including small molecules and polymers, offer the advantage of molecular design for achieving specificity to specific analytes.[6–8] Moreover, the strong dependence of the physical properties of these organic building blocks on external conditions allows the fabrication of a wide range of sensors such as temperature,

radiation, pressure, and chemical, among others.[7,9–13] These transducers can be used to monitor vital internal body parameters related to healthcare[14–16] or external ones such as environmental agents (both hazardous and vital ones),[7,8] opening the possibility for an entire sensing ecosystem. Among the different types of possible sensors, organic gas sensors pose an attractive near future and more realistic possibility for their implementation in commercial devices. Some of the major drawbacks associated with the use of organic semiconductor molecules are their chemical degradation (stability) against some gaseous agents and long-term reliability issues.[6,17–20] However, in contrast to their inorganic counterparts, organic molecules offer enormous structural flexibility and diversity through molecular engineering, which, along with improved device fabrication, offers the chance to overcome these problems. Moreover, they can exhibit considerably higher sensitivity and selectivity, lower operation temperature (even at room temperature operation), and shorter response and recovery time than commonly used metal oxides.[21–23]

Organic π-conjugated small molecules such as phthalocyanines have been one of the most studied families of organic semiconductors in gas sensing due to their tailorable chemical structures, mechanical flexibility, and good chemical and thermal stability.[24–26] These molecules are processable in vacuum to produce high-quality amorphous or crystalline films on various substrates, further facilitating the fabrication of sensing devices. The conductivity of phthalocyanine films (the

ARTICLE

great majority are p-type semiconductors) at room temperature in air is relatively low, but when temperatures are raised above 100 ºC, the conductivity increases significantly.[27,28] The exposure of metal phthalocyanines (MPcs) to electrophilic gases such as NO_x, Cl_2, F_2, BF_3, or O_2 produces an increase on the holes concentration in the film and a consequent increase in conductivity.[29–31] On the other hand, reducing gases, such as NH_3, tend to decrease the conductivity attributed to electron donation from the reducing gas to trap charge carriers.[27,28] The interaction of analytes with the metal center in metallophthalocyanines (MPcs) modifies the material's charge distribution, altering its resistance and enabling gas detection.[27–34] Furthermore, the metal center's electronic properties can be tailored to optimise the sensor's response to specific gases. For instance, zinc phthalocyanine (ZnPc) has shown potential in detecting complex analytes, including chemical warfare agents.[35] The rational selection of the metal center, combined with the conjugated structure of phthalocyanines, contributes to the selective and sensitive detection of various gases.[27–34]

In the case of metal-free phthalocyanine (H_2Pc), it is hypothesised that electrophilic species, including oxygen, are adsorbed on the molecules by weak interactions with the four meso-nitrogens or by hydrogen bonds to the two inner hydrogens, leading to a slight conductivity increase, although not as pronounced as in MPcs.[27–34] The adsorption of analytes to phthalocyanines is considered to occur exclusively at the very surface of the films due to steric hindrance related to the tightness of the phthalocyanine crystal structure.[27,36] In this sense, phthalocyanine nanowires (NWs) should provide a unique opportunity to enhance the sensing properties of these compounds owing to the larger surface area exposed to the analyte compared to the usual thin film approach.[13,29,37] However, most studies on phthalocyanines as gas sensors are restricted to thin films or the single-wire field effect transistor (OFET) operation.[24,38–41] This latter approach, although with proven advantages such as high sensitivity and field-driven tunable selectivity, fails in a readily large-scale application since it relies on expensive and multistep procedures, including the synthesis of the transductors, photo or electron beam lithography and/or nano-handling of the organic nanowires to build the sensor device.[42–45]

In such a context, we demonstrate herein a highly reproducible and affordable methodology for fabricating gas sensors consisting of high-density arrays of H_2Pc single crystalline organic nanowires (ONWs) synthesised by vacuum deposition on metallic electrodes. Our protocol has been exploited in the last years for the growth of ONWs on processable and functional substrates such as metal (Au, Ag and Cu) and metal oxide (TiO_2, ZnO, SiO_2, FTO, and ITO) on silicon wafers, fused silica plates or polymeric supports (PDMS, PET).[46–57] Thus, contrary to most of the results in previous literature, where the transfer of the 1D nanomaterials to different substrates to assemble the sensors is usually required,[29,42–45,58] here we present the direct fabrication of ONWs on Pt interdigitated substrates decorated with gold nanoparticles. It is important to outline that the sensor mechanism itself is not intrinsically dependent on the use of Pt or Au. In practical applications, cost-effective alternatives, such as other low-cost nanomaterials (Cu, Al), could replace these components without significantly compromising sensor performance. In addition, we explore different strategies to increase sensor sensitivity. We compare the single crystal nanowire array sensor response to electrophilic (O_2) and inert (Ar) gases with the performance of high surface-area organic nanotrees (ONTs) and highly interconnected wires processed by introducing an additional liquid evaporation route. Finally, organic nanowires and nanotrees serve as model systems to study the enhanced response of the sensors provided by illumination with white or monochromatic light to the organic semiconducting systems.

Experimental

Sensors fabrication. Commercial electrodes (Micrux) with 15 pairs of interdigitated Pt microelectrodes separated by 10 µm were used as received. Pt electrodes were chosen primarily due to their stability, reproducibility, and ready availability in our laboratory. While alternative, cost-effective metals such as Cu or Al could also be employed, Pt offers a significantly lower surface oxidation state, which is advantageous for research purposes. Before the sublimation of H_2Pc, gold seeds were deposited to provide the necessary roughness for the growth of ONWs.[46–49] The metallic seeds were deposited by magnetron sputtering under Ar atmosphere at 0.1 mbar employing an Emitech K550 sputter coater equipped with a gold target of 60 mm diameter. The use of Au nanoparticles on Pt electrodes promotes the formation of discrete nanoparticles due to favorable wetting characteristics, unlike Au on Au substrates (for example, in case Au electrodes are chosen), which often result in thin films. To avoid conduction through the Au NPs, the deposition was performed at 12.5 mA for 10 seconds, assuring the formation of isolated nanoparticles on the pre-patterned electrodes (see Figure S1 in the Supplementary Information). For the sublimation of H_2Pc (29H,31H-Phthalocyanine, Sigma-Aldrich, 98% purity), the base pressure was 10^{-6} mbar, and the Ar pressure during deposition was set to 0.02 mbar. A Knudsen-type cell was used for the sublimation (model LTE 01 supplied by Kurt J. Lesker), and the temperature was controlled to obtain a constant deposition rate of 0.5 Å/s measured by a quartz crystal monitor (QCM). The sample-to-evaporator distance was 6.5 cm, and the substrate temperature was 170 ºC. The nominal thickness of the primary ONWs was set to 3 kÅ (measured by QCM).

For the growth of the Organic Nanotrees,[46–48,50] the primary ONWs were used, and a first oxygen plasma treatment of 20 minutes at 300 W was applied using a microwave plasma source ECR-SLAN operating at 2.45 GHz (Plasma Consult Gmbh). The total oxygen pressure was 0.02 mbar, with the substrates at room temperature, and the samples-to-plasma distance was set to 10 cm. The oxidative plasma treatment was followed by the growth of secondary ONWs using the same conditions as before but reducing the thickness to 1.5 kÅ (QCM). The as-grown ONWs were compared with highly interconnected nanowires obtained after solution post-treatment by immersion in water and subsequent drying. The final sensor was attached to the

feedthrough, welding copper wires for the electrical connections, and inserted into the measurement chamber (see Supplementary Information Scheme S1).

Characterisation Techniques. SEM micrographs were acquired in a Hitachi S4800 working at 2 kV on samples prepared on Si (100) Substrates. Cross-sectional views were obtained by cleaving the substrates. The ONWs and ONTs were dispersed onto Holey carbon films on Cu grids from Agar scientific for TEM characterization. High resolution TEM was conducted with a FEI Tecnai Osiris TEM/STEM 80-200 operating at 200 kV. Raman spectra were acquired using a Horiba Jobin-Yvon LabRAM spectrometer equipped with a confocal microscope with a 50x objective and a laser of 532 nm wavelength, with a spectral resolution of ~ 1.7 cm^{-1}. Low laser powers were utilised to prevent H_2Pc damage. XPS characterisation was performed in a Phoibos 100 DLD X-ray spectrometer from SPECS. The spectra were collected in the pass energy constant mode at 50 eV using an Mg Kα source. C1s signal at 284.8 eV was utilised to calibrate the binding energy in the spectra. The assignment of the BE to the different elements in the spectra corresponds to the data in references [59,60].

Sensors characterisation. The electrical characterisation of the sensors and their response evaluation were performed with a Keithley 2635A system source-meter working in sweep voltage mode for the I-V curves and temporal evolution at a fixed potential of 5 V for the sensor response. The sensor is housed in a small, heatable chamber with an approximate volume of 50 cm^3. Gases were introduced into the chamber using two calibrated mass-flow controllers (Bronkhorst), each set to deliver argon (99.99%) and oxygen (99.99%). Argon (Ar) was selected over other inexpensive inert gases, such as nitrogen, due to its higher chemical inertness, minimizing potential interference and ensuring that observed signal variations originate from the analyte (O_2) rather than the carrier gas. Both Ar and O_2 were supplied at a flow rate of 100 sccm, facilitating rapid atmospheric transitions within the chamber. A needle valve with minimal aperture was installed at the outlet to prevent gas backflow. The chamber features a fused silica window, allowing for light illumination experiments. Heating of the chamber was achieved using an electrical resistance, with temperature monitored by a K-type thermocouple. Two different light sources were used, one a high-intensity Xe lamp (LASING ASB-Xe-175) and a second multi-LED source (DiCon, Microscope Illuminator, MSB-MX-25) equipped with 3 LEDS (blue, green and red). The light power density was measured with a radiometer (Solarlight PMA21) at 5 cm from the samples at two different spectral ranges: UVA+UVB (detector PMA2107) and Vis + NIR (PMA2140).
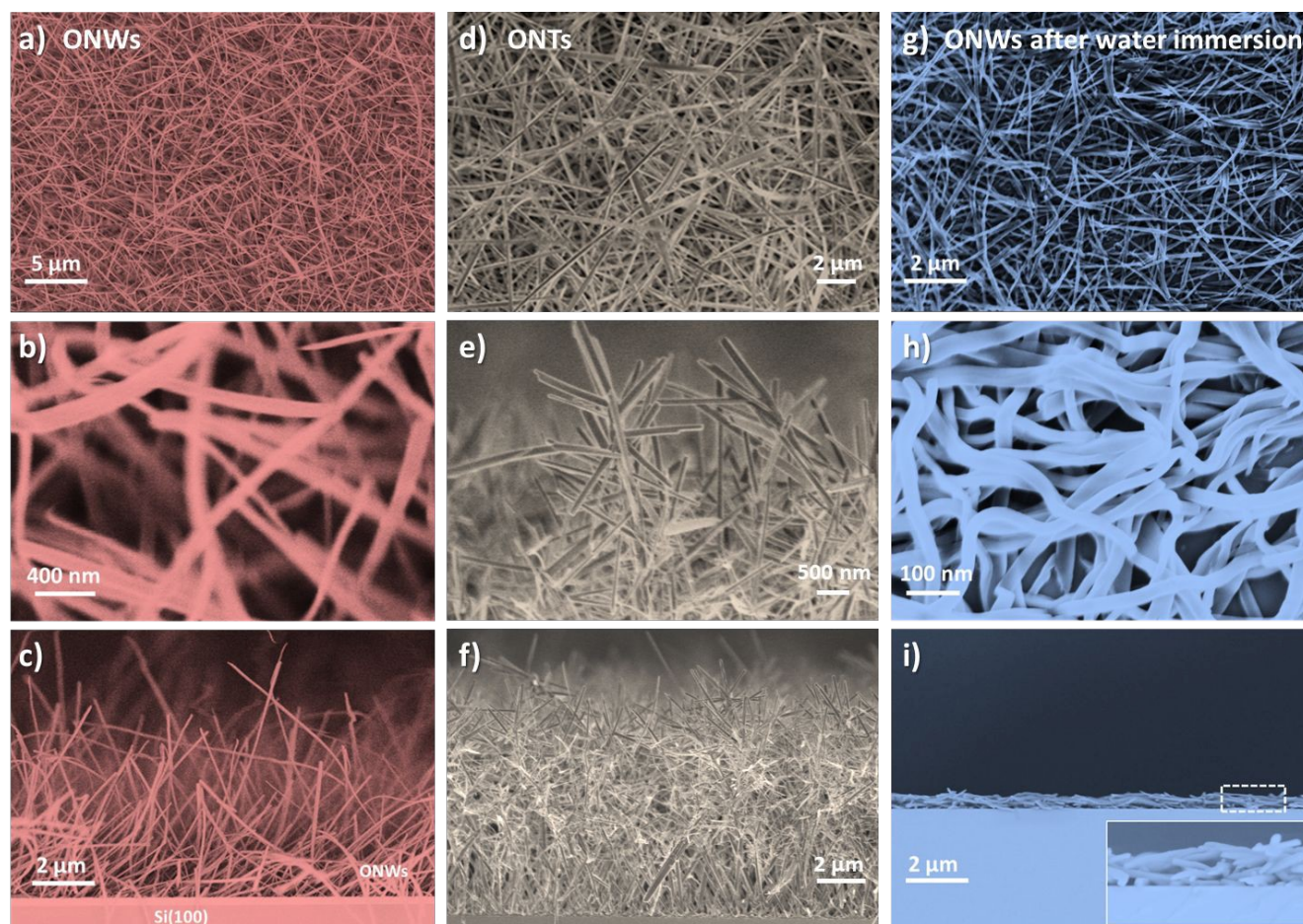
Figure 1. a-c) SEM micrographs of the H_2Pc ONWs deposited on a silicon wafer decorated with a thin gold film with planar views in panels a-b) and cross-section in panel c). d-f) SEM micrographs in planar view (d) and cross-section (e-f) of the H_2Pc ONTs. g-i) Characteristic SEM micrographs of the supported ONWs after immersion in distilled water.

The relative response (R) of the sensor was calculated using the relation:[61]

$$R(\%) = \frac{Resistance\ (gas) - Resistance\ (initial)}{Resistance\ (initial)} \cdot 100$$

Results and Discussion

In this article, we have taken advantage of a previously reported vacuum deposition procedure for fabricating high-density arrays of supported organic nanowires.[46–57] This high throughput method yields the growth of single crystalline nanowires by self-assembly of planar and non-planar small molecules with high purity, growth rates, and homogeneity. A scheme for the growth of ONWs is shown in Scheme S1 in the Supplementary Information section. In references [46–57], the growth of perylene-, metal and free phthalocyanines- and porphyrins-NWs supported on metal, metal oxide, polymeric and organic surfaces has been demonstrated and optimised. The growth mechanism responds to a combination of the single-crystalline structure formation promoted by the uniaxial anisotropy of the molecular self-assembly by pi-stacking.[46,47]

Thus, Figure 1 a-c) show typical SEM images of the metal-free phthalocyanine (H$_2$Pc) NWs formed on a Si(100) wafer decorated with Au nanoparticles. Lengths and widths of the ONWs are between 2 to 10 µm and 20 to 100 nm, correspondently. As detailed in previous works,[46,47,62] the ONWs growth requires the presence of nucleation sites that can be added to the electrodes in the form of nanoparticles or thin films with a certain roughness. In this work, these required nucleation sites have been added as gold nanoparticles (NPs), ensuring no coalescence between them and, therefore, no electrical contact. A representative SEM image of the Au NPs distribution is shown in Figure S1.

The present approach aims to connect two preformed electrodes through the ONWs. Since the electrical connection is produced by the physical contact of two isolated wires growing from each electrode and aiming to increase the surface area, a highly branched organic nanotree architecture was used (Figure 1d-f). A detailed report on the fabrication of such three-dimensional nanostructures can be found in references [48,50]. The procedure consists of using the primary ONWs as support (i.e., acting as trunks) to form secondary ONWs (playing the role of branches). A soft-plasma etching treatment is carried out on the as-grown (primary) nanowires to generate a certain roughness that serves as the nucleation site for the formation of the secondary wires. Thus, as Figure 1 (d-f) presents, the density of ONWs is increased by more than an order of magnitude. Moreover, the lateral connectivity of the ONWs layer is also improved through multiple contacts between primary, secondary, and adjacent secondary ONWs. It is important to stress that the nanowires are single-crystalline for both configurations, 1D and 3D. Figure 2 shows the high-resolution TEM image of an H$_2$Pc nanowire (a) and the interconnection between primary and secondary nanowires forming a nanotree (b). The ONWs present the characteristic

stripped pattern of the single-crystalline configuration corresponding to the self-assembly π-stacking growth mechanism along the nanowire length. The crystallinity is also evident from the Digital Diffraction Pattern (DDP) at the right of the figure for the indicated area, where both the primary and the secondary ONWs present two maxima corresponding to the periodicity of the row of molecules visible in the TEM images. It is worth mentioning that the FFT image of the secondary wire presents four maxima, which are due to a change in the crystalline orientation at the vicinity of the branch (see the green circle in Figure 2b), likely due to the presence of a dislocation. In the case of the connected ONWs, the plasma etching process to generate the nucleation centres for the formation of the secondary branches was soft enough to keep a low roughness of the surface of the primary nanowire but likely produced an amorphous shell along the ONW. Please note that the thickness of such an amorphous shell is extremely difficult to characterise as the ONW crystalline structure gets easily destroyed under the electron beam.[46–48,54,63]

Raman and X-ray photoelectron spectroscopy (XPS) were employed to validate the structural and elemental composition of the phthalocyanine nanostructures, which are shown in the Supplementary Information S2 and S3, respectively. Both techniques reveal that ONWs present a high purity from both the structural (from Raman) and chemical (from XPS) points of view. Further insights provided by XPS have been also included in the Supplementary Information S3.

It is worth stressing that the ONWs and ONTs growth methodology only involves dry vacuum steps of deposition and processing. In this article, and for the sake of comparison with other results in the literature, we have included an additional post-processing step, the immersion of the nanotrees in a solvent, in this case, distilled water (and the subsequent drying), to enhance the lateral connectivity further. As shown in Figure 1 g-i), the water immersion significantly increases the number of interconnections between the ONWs. This is particularly clear in the cross-section image (i), where all the ONWs lying down close to the surface of the substrate can be observed.

Figure 3 a-b) shows SEM pictures of the commercial Pt interdigitated electrodes used for the sensor fabrication at different magnifications. A brighter appearance for the metal can be noted, where the fingers of the interdigitated electrode are separated 10 µm. Figure 3 c) shows the ONTs grown onto the preformed electrodes (as detailed in Scheme S1 in Supplementary Information), where the high density of 1D nanostructures and the connectivity achieved can be observed. The metallic electrodes are partially visible behind the ONTs and can be noted with a different contrast in the SEM image of Figure 3 c). Our methodology enables the direct growth of ONWs and ONTs onto preformed electrodes at temperatures below 200°C, eliminating the need for transfer steps and enhancing key factors such as electrical contact and reproducibility. Unlike most existing studies, which require higher temperatures, post-synthesis assembly or templated substrates,[13,29,42–45,58] our approach achieves superior nanowire density and connectivity. While some prior works have demonstrated direct deposition on preformed devices, the

resulting nanowire networks exhibit significantly lower density and interconnectivity.[37,64] In contrast, our method integrates a highly connected ONW network onto interdigitated electrodes. Additionally, the unique architecture of the branched ONTs, combined with an immersion-based strategy, further improves electrode bridging and enhances conductive pathways.

Figures 3 d) and e) present the I-V characteristics of ONWs (d) and ONTs (e) at RT (black curve) and 100ºC (red curve). The I-V characteristics are nearly linear in all cases, indicating fair electrical contact between the nanowires and between the nanowires and the electrodes. This effect may have two different origins: i) one is the match between the Highest Occupied Molecular Orbital (HOMO) of H_2Pc and the work function of gold nanoparticles (used as nucleation centres to grow the ONWs), which are 5.7 eV[65] and 5.5 eV[66], respectively; ii) the second is the excellent interface in terms of cleanliness (the ONWs or ONTs are entangled while are growing in vacuum), that ensures excellent contact between the wires.
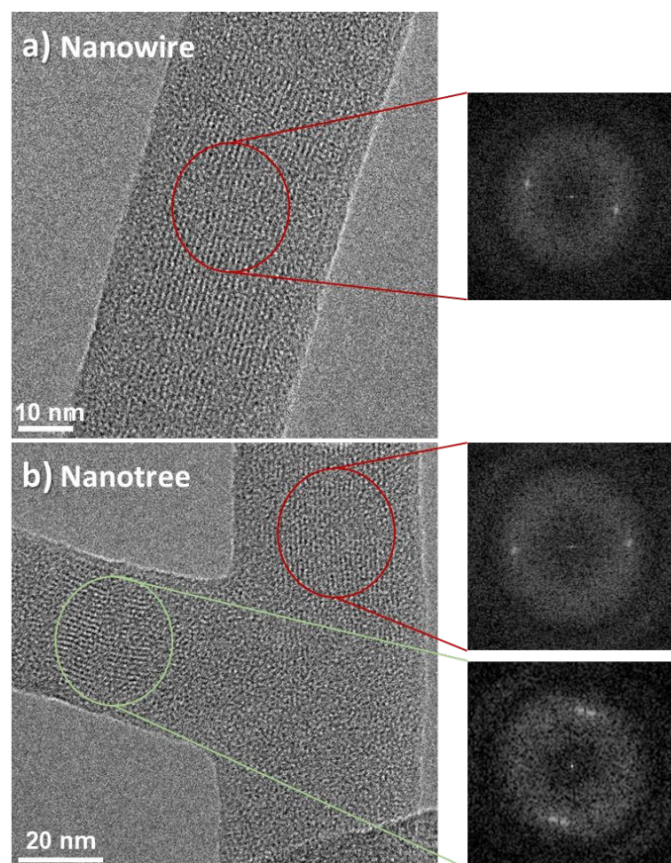
Figure 2. High-resolution transmission electron micrographs corresponding to an H_2Pc nanowire (a) and the connected primary and secondary wires in an H_2Pc nanotree (b). Digital Diffraction Patterns (DDP) of the selected areas (right side of the figure) reveal the crystalline character of the ONWs and ONTs.

The samples are highly resistive at room temperature, as noted in the I-V curves of Figure 3 d-e) (note that the measurements have been performed under Ar flux). The current flowing through the ONWs barely reaches 10^{-10} Amperes at 5 Volts, yielding a high resistance of 18.7 and 57.6 GΩ for ONWs and ONTs, respectively. Such a high resistance can be understood

due to the high intrinsic resistivity of the H_2Pc molecule and due to the low cross-section of the ONWs, though, to the best of our knowledge, the resistivity of ONWs of H_2Pc has not yet been reported. Supplementary Information S4 provides an estimation of the number of contacts between ONWs in adjacent electrode fingers to contextualise our results within the current literature.

It is noticeable that the measured resistance for the ONTs is higher than for ONWs. The nanowires and nanotrees have been prepared under the same experimental conditions, since the ONWs are used as the initial trunk for the ONTs, and the only difference is an additional plasma treatment and subsequent deposition of the branches. Thus, the number of possible contacts between the trunk or the branches of the ONTs needs to be higher than for the ONWs. Thus, the higher resistance value can be understood as an increase in the contact resistance between the nanotrees or by a deterioration of the conductivity of the initial trunk, surely related with the amorphisation of the primary ONWs outer shell discussed in Figure 2, both effects arising from the plasma treatment. This is also consistent with the Raman spectrum of ONTs shown in Figure S2, that shows a noisier Raman spectrum, ascribed to surface amorphisation induced by the soft plasma treatment.

Although the oxygen treatment and subsequent growth of secondary branches in the ONTs may appear to be a stochastic process, the ONT-based sensors synthesized in this study exhibit a similar resistance. The resistance measured in similar conditions (RT and Ar atmosphere) for three different ONTs-based sensors synthesized in different batches have been included in Table S1 in the Supplementary information. This suggests a level of reproducibility in their electrical properties, despite the seemingly random nature of the structural modifications induced by the treatment.

By contrast, the resistance of the ONWs drops significantly with temperature, decreasing from 18.7 and 57.6 GΩ to 0.99 and 0.59 GΩ for ONWs and ONTs, respectively. It is worth mentioning that this change in the resistance induced by the temperature is a reversible phenomenon, as can be observed in Figure S5. The resistivity of a semiconductor ONW or ONTs is anticipated to decrease with temperature due to the electronic population of the Lowest Unoccupied Molecular Orbital (LUMO) levels. However, the observed reduction is much higher than the expected decrease in resistivity, which has been reported to decrease to half for H_2Pc thin films (from ca. 2 to $1 \cdot 10^6 \ \Omega \ m$).[28] The decrease in the resistance from RT to 100ºC for the ONW devices is about 15 times, while for the ONTs, this decrease is significantly enhanced, reducing their resistance by almost two orders of magnitude at 100ºC. Those results are consistent with an overall decrease in the contact resistance between the wires induced by the temperature and would indicate that the number of contacts is higher in the case of the nanotrees (as expected) since the final resistance is lower for the ONTs at 100ºC. Following this reasoning and considering the higher number of contacts in the nanotrees-based device, we immersed the samples in water to increase the contacts between the ONWs or ONTs, as shown in Figure 1 g-i). As expected, the resistance can be further decreased for the ONWs

Nanoscale Accepted Manuscript

ARTICLE

from 0.99 to 0.64 GΩ and more for the ONTs from 0.59 to 0.16 GΩ. Even though the resistance values might seem high, it must be kept in mind that the conduction is achieved through a hopping mechanism between NWs. Thus, the device's resistance can be decreased by shortening the distance between adjacent electrodes and/or increasing the hyperbranching. Due to the lower resistance of the most branched structures, all the sensors studied will be based on nanotrees.
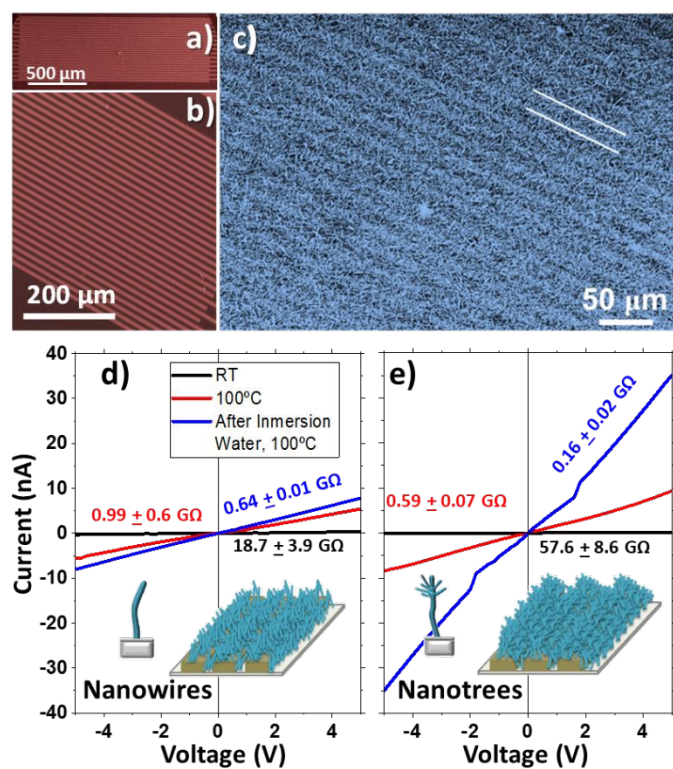
Figure 3. a-c) SEM image of the commercial interdigitated electrodes before (a-b) and after (c) the deposition of H_2PC nanotrees. d-e) I-V curves for ONWs (d) and ONTs (e) on commercial electrodes at Room Temperature (black) and 100ºC (red) under constant argon flux at ambient pressure. In addition, the I-V response of the device is shown after the water immersion treatment and the subsequent drying. These curves were recorded at 100ºC under Ar flux (blue curves).

As previously reported, the optoelectronic properties of the phthalocyanine are modified when exposed to oxygen or oxidising gases present in the surroundings.[24,40,67,68] However, the oxygen response is usually very slow for phthalocyanine-based sensors at room temperature, requiring their operation at elevated temperatures.[24,40,67,68] In line with the literature, the RT response of the ONWs or ONTs is barely noticeable to the change in the gas atmosphere from argon to oxygen. The response is shown in Figure 4 a) and magnified in b) (black lines), which show the change in the I-V curves after 10 minutes of pure oxygen and argon flow, with a minimal change in the resistance (from 19.9 to 23.3 GΩ, respectively). By contrast, Figure 4 a) shows how the response at 100ºC is significantly enhanced, producing a decrease in the resistance from 1.0 to 0.49 GΩ for argon and oxygen environments, respectively. It is worth highlighting that the I-V curves were recorded after 10 minutes of oxygen or argon flow since prolonged times

(especially under a pure oxygen atmosphere) produced a significantly higher decrease in the resistance of the devices. This effect can be seen in Figure 4 c,d), where the initial resistance decrease is due to a 1-hour exposure to a pure oxygen atmosphere. Figure 4 c) and d) show the resistance of the device when the gas atmosphere is changed from pure Ar to O_2 at 100ºC (c) and RT (d), respectively, at intervals of 5 minutes, imposing in all cases a bias of 5 V to the sensors. While switching the gas flux into the chamber from Ar to O_2 at RT only produces a slight modification of the resistance of the device (Figure 4d), the variation at 100ºC is significantly enhanced (Figure 4 c). Despite the increased response of H_2Pc thin films to oxygen for high temperatures, a known behaviour for this organic semiconductor, it should be barely noticeable at 100ºC, as reported by other authors.[67,69] By contrast, this study demonstrates a marked resistance response of H_2Pc ONTs against oxygen at 100ºC. The reported low response is usually attributed to the slow diffusion of the oxygen in a thin film, since it is expected to be much slower than in our branched structure. Thus, the much higher surface area exposed by the nanotrees, effectively enhance the doping effect of oxygen and increases the response of the ONTs-based sensor.
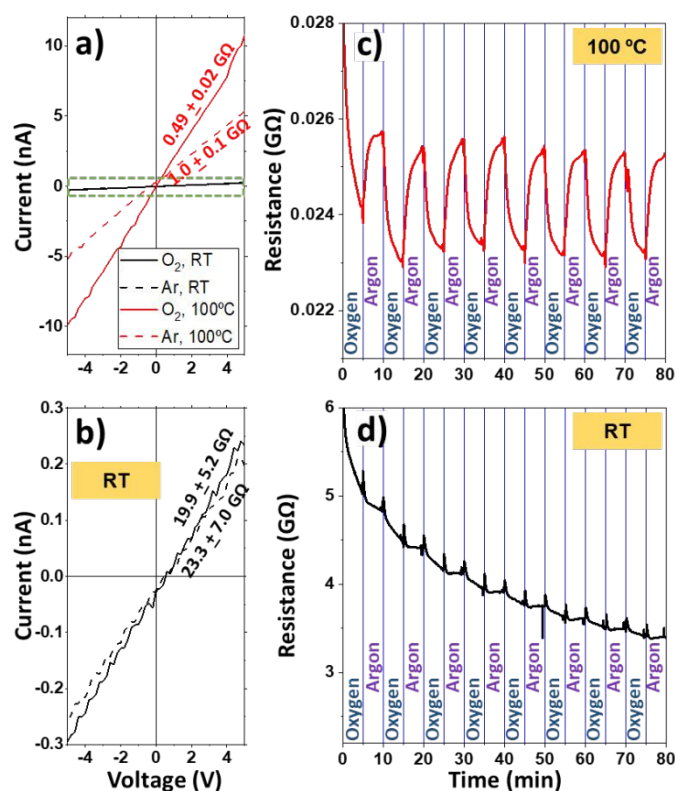
Figure 4. a) I-V curves for ONTs deposited on commercial interdigitated electrodes at Room Temperature (black) and 100ºC (red) under constant oxygen (solid line) or argon flux (dashed line) at ambient pressure. b) Zoom of I-V curves at the highlighted area in a) to reveal the lack of response at room temperature. The curves have been recorded after 10 minutes of argon or oxygen flux. c-d) Resistance variation vs time for the ONTs grown onto interdigitated electrodes at 100º (c) and RT (d). The system was dosed with pure oxygen for 1 hour and cyclically exposed to argon and oxygen for 5 minutes.

The response of the ONTs-based sensors to oxygen/argon cycles was evaluated at different working temperatures and

under combined irradiation. The response of the sensor upon the illumination with a Xenon lamp is shown in Figure 5 at RT (a), 50ºC (b), and 100ºC (c) with red curves (labelled as UV+Vis). To discern the effect of the UV portion of the Xe lamp, a long-pass filter with a cut-on wavelength of 400 nm was used to illuminate the sensor (blue curves in Figure 5 labelled as Visible). As mentioned in Figure 4 d) for the room temperature case (Figures 5 a and c show the same curve as Figure 4 d and c, respectively, for comparison with the illuminated cases), by alternating between oxygen and argon flows, a very subtle saw-like resistance response was obtained, that are even masked by the noticeable drift in the curve. Upon visible light irradiation, the resistance decreases by three orders of magnitude, and an enhanced sensor response can be noted due to light activation. This light activation arises due to the electronic population of the LUMO levels (as it occurs with temperature) inherent to the semiconductor nature of the molecules for light energies above the H_2Pc band gap of 1.88 eV.[70] On the other hand, UV+visible light does not produce any further resistance change compared to irradiation in the visible range. This behaviour is likely due to the tiny difference in power density of the visible and UV+visible radiation, which is roughly 73 mW/cm^2 (Table S2 in Supplementary Information). Note that near-infrared radiation (NIR) was not eliminated from the light source, however, it should not affect the measurements due to the higher band gap of H_2Pc. In addition, it was corroborated that NIR radiation did not produce any significant change in temperature during measurements, as evidenced by the thermocouple.

Rising the temperature to 50 ºC (Fig. 5 b) and 100ºC (Fig. 5 c) further decreases the resistance of non-illuminated sensors by more than two orders of magnitude when comparing the 100ºC to the RT case. Besides, the drift observed in the RT case for non-illuminated sensors is decreased at 50ºC and is no longer present at 100ºC. Moreover, the sensor response reveals that the saw-like features of the curves were much more defined as temperature increased, demonstrating again the role of temperature in the sensor performance. By contrast, the illumination of the sensors at 50ºC (b) and 100ºC (c), both with and without the UV component, produces a decrease in the resistance similar to the one encountered for the RT. It is worth highlighting that the three graphs (a-c) present the same resistance range at the illuminated region (before the break of the graph), facilitating the comparison between the different temperature cases. These results indicate that the illumination effect on the conductivity is more pronounced than the increase in the temperature up to 100ºC. This is due to the high power of the lamp used, which has a total power of 1.77 W/cm^2 (Table S2). For the sake of comparison, Figure S6 gathers the sensor response to oxygen and argon for the three temperatures employed in Figure 5 in the dark and under illumination. The resistance is graphed on a logarithmic scale and is the same for the three studied temperatures. The figure clearly shows that the effect of the illumination on the conductivity is almost independent of the temperature of the samples. This suggests that potentially low-cost and long-lifetime sensors can be realised since room temperature operation reduces the degradation time of organic-based sensors. It is worth

mentioning that although the sensing capability of the sensor is clearly enhanced by visible (or UV+visible) illumination, the shape of the curves is not perfectly defined. It first shows a sudden decrease (which is reduced in magnitude as temperature increases) to the change from O_2 to Ar and then a constant increase that is sometimes significantly delayed. This latter feature makes the sensor respond the opposite way (Visible illumination at RT and 50ºC, blue curves in a-b).
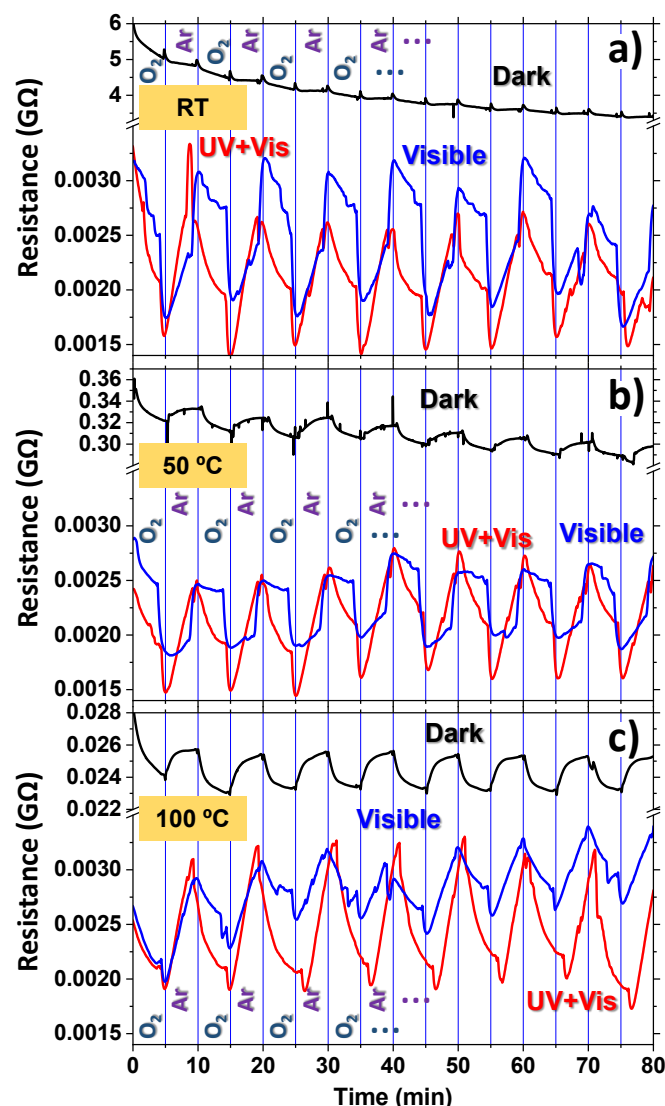
Figure 5. Organic nanotree sensor response to oxygen and argon at RT (a), 50 °C (b), and 100 ºC (c), under no irradiation (black line), visible light (blue), and UV+visible light (red).

It may be stressed again that in Figure 5, the photoconductivity and the enhanced response of the phthalocyanine ONTs have been tested using an Xe lamp with high power (>1700 mW cm^{-2}). To unravel the possible use of the sensor under more feasible light sources with lower power, we tested them under Light Emitting Diode (LED) illumination.

As demonstrated in Figure 5, light-induced responsivity can be used to switch ON and OFF the sensor response, consequently increasing their lifetime. To prove this idea, illumination experiments were carried out using a series of three LEDs: blue,

ARTICLE

green, and red at emission wavelengths of 465, 530, and 635 nm, respectively, with significantly lower powers than the Xe lamp used in the previous experiences (see Table S2). The switching evolution is shown in Figure 6 a) and was measured at 100 ºC under a constant oxygen flux atmosphere for the ONT-based sensor. It may be appreciated that once the LEDs were turned ON, the resistance jumped down quickly, and when turned off, the contrary occurred. Note that the resistance changes were not as pronounced as in the previous case due to the lower power of the LEDs. The bottom part of the Figure 6 a) shows the relative response calculated from the previous curves. To minimise the drift effect, the relative response has been calculated by using the signal some seconds before the illumination change and after 20 seconds. For every LED, two different responses were obtained separately, distinguishing between the "Off-On" and "On-Off" transitions (note that these transitions occur at 5,15,25 and 10,20,30 minutes, respectively). The change in the sensor's response is not identical for the two cases, as it can be observed in the figure. The relative response is systematically lower for the On-Off steps for the three LEDs. One remarkable characteristic is that the H_2Pc presents a visible absorption band at 620 nm, very close to the red LED wavelength, as shown in Figure S7. From this figure, noticeable changes in the resistance evolution for the different wavelengths of the LEDs are expected since the H_2Pc ONTs absorb a significantly smaller amount of light at the green and blue wavelengths than the red one. According to the UV-Vis transmittance and the emission spectra of the LEDs (both shown in Figure S7) and the power densities listed in Table S2, the red LED should report the highest photoconductivity, but this has not been the case. While the responses are comparable, the red LED consistently produces the smallest response, and the green LED produces the highest change across all cycles, regardless of whether the transitions are "On-Off" or "Off-On." This behaviour does not correlate neither with the absorption band of the ONTs nor with the power of the LEDs, indicating that adittional efects such as the sensor drifting need to be considered.

The response times for the sensor upon illumination with the three LEDs has also been calculated by fitting with a two-exponential decay curve, which are shown in Figure S8. For all wavelengths studied, similar response times were observed, with two distinct components: t1 (faster) and t2 (slower), the latter with the highest contribution (more than 95% for all the cases). As occurred with the relative responsed of Figure 6a), the response times differed significantly between the "Off-On" and "On-Off" transitions, with the latter showing slower t1 and faster t2. It should be noted that drift may influence these fits, specially the differences between "Off-On" and "On-Off" transitions, and therefore the response times should be interpreted qualitatively.

Since no significant wavelength dependence was observed (neither in the relative response nor the response times), the photoconductivity experiences with LEDs were performed using a combination of the three previously used LEDs (R+G+B), giving an overall power density of 11.2 mW/cm² (See Table S2). Figure 6 b) presents the I-V characteristics of the ONTs-based sensor

before (green lines) and after water immersion (black and red lines), both under white LED illumination (black) and in the dark (green and red) at 100ºC. As mentioned, the immersion process induces an improved interconnection between the branches, producing a significant decrease in the resistance of the sensor device, from 0.48 to 0.1 GΩ, which is further decreased to 0.04 GΩ under white LED illumination (measured in an oxygen atmosphere). Figure 6 b) also shows the I-V curves under O_2 and Ar atmosphere (after ca. 10 minutes of exposure) with solid and dashed lines, respectively. Though the first impression from the figure is that the illuminated ONTs after water immersion show the highest variation, the three cases have approximately the same response of about 35-45% when the atmosphere varies between argon and oxygen (in this case, no precise response could be given due to the lack of measurement cycles). This would indicate that although the resistance is lower for devices treated by immersion in water and under LED illumination, the response is similar for the three cases.

The resistance evolution under intermittent LED illumination (every 5 minutes) is presented in Figure 6 c) and d) before and after water immersion, respectively. Please note that the starting resistance is not as low as in the previous Figure 6 a) because the white LED experiments performed at 100ºC started 10 minutes after reaching the target temperature, while in the rest, the stabilisation time was above 1 hour. The figure shows the evolution of the sensor at RT (black curve) and 100ºC (red). It can be noted that there is a fast resistance change upon illumination in all cases, where the change is significantly higher for the RT experiences. In these measurements at RT (black curves in Figures 6 c-d), the resistance difference between the OFF/ON states (understanding the sensor as a photodetector) gives a response of 87 $\pm$ 2 and 89 $\pm$ 2 %, while at 100ºC (red curves) is 68 $\pm$ 5 and 61 $\pm$ 6 % for the devices measured before and after water immersion treatment, respectively. These results are similar to those shown in Figures 5 and 6 a) and consistent with photoconduction switching, which has also proven to be prompt and reproducible with the light turning on and off (Figure 6 c-d), implying not only fast photoresponse but also the high stability of the materials when operated under ambient conditions.

The reported photoconductivity can be used to decrease the resistance of the sensor devices, but is the sensitivity of the sensor modified upon LED illumination? To answer this question, Figure 6 e-f) shows the evolution of the resistance under continuous white LED illumination upon modifying the atmosphere from oxygen to argon (cycles of 5 minutes) at RT (black curve) and 100ºC (red curve) before (e) and after (f) the water immersion treatment. Starting from the 100ºC experiences, the resistance evolution depicts a similar shape than shown in 5 c) for the Dark case. The main difference is a higher sensitivity in the white LED illuminated experiences for both before and after water immersion treatment, showing a response of 37 $\pm$ 2 and 35 $\pm$ 4 %, respectively, while in the dark case (only measured before water immersion treatment, as it is shown in Figure 5 c) shows a four times less response of 9 $\pm$ 1 %. This experience proves that LED illumination enhances the sensor response.
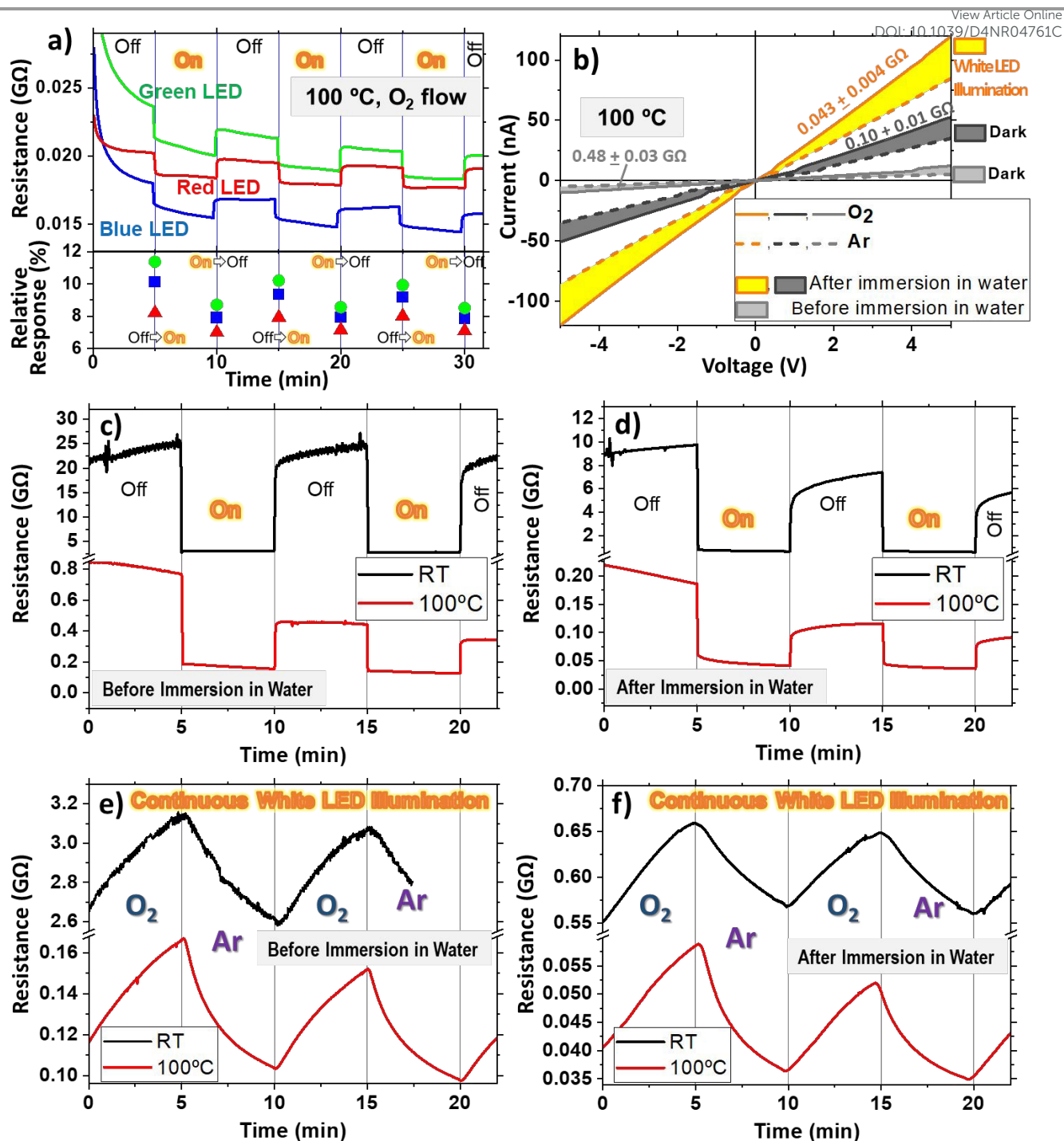
Figure 6. a) Sensor response at 100 ºC to oxygen under intermittent illumination with red, green or blue LEDs (top) and Relative Response (bottom). b) I-V curves of the ONTs sensors before (green lines) and after water immersion treatment (black and red lines), both under white LED illumination (black) and in the dark (green and red) at 100ºC. The I-V curves under O_2 and Ar atmosphere (after 10 minutes of gas flow) are shown with solid and dashed lines, respectively. c-d) Resistance evolution of the sensors at a constant O2 flow at RT (black line) and 100 ºC (red) under intermittent LED illumination every 5 minutes before (c) and after (d) water immersion treatment. e-f) Resistance evolution under continuous white LED illumination upon modifying the atmosphere from oxygen to argon in cycles of 5 minutes, at RT (black curve) and 100ºC (red curve) before (e) and after (f) the water immersion treatment.

Moreover, the RT experiences revealed a striking result: while in the Ar/O_2 cycling experiments in the dark, the sensor shows no response (not possible to quantify), the illumination with a low-power LED enables the sensing capability of the devices. The illumination increases the response from nearly zero to 16 $\pm$ 1 % and 14 $\pm$ 1 % before and after water immersion treatment,

respectively. It is important to remark that the enhanced response for the RT case under a low-power white LED illumination proves that the sensor can be switched ON and OFF by simply illuminating with an LED together to a reduction of the resistance. To our knowledge, these are the first results of a visible range lighting strategy to improve the response of the

Journal Name

organic-based sensors, opening a new path toward the exploitation of semiconducting organic nanowires as low-cost and low-power sensors since they can be switched on and off periodically simply by illumination with a LED, diminishing their consumption since they can operate at RT.

Conclusions

The direct fabrication of H_2Pc nanowires and nanotrees on preformed interdigitated-based sensors has been successfully addressed. A high-density nanoforest was obtained by a combination of vacuum/plasma deposition methods, namely magnetron sputtering for the seeds, physical vapour deposition for the nanowires and soft plasma etching for the formation of crystallisation sites along the primary ONWs to induce the growth of secondary ones. The entire process has been carried out at mild temperatures (< 200 ºC) on commercial substrates consisting of interdigitated electrodes, reducing resistivity due to the contact of the ONW or ONTs. The resistance was significantly lower for the ONTs sample, indicating a higher number of contacts between the branches. The nanowire contact could be further improved by a simple water immersion protocol for both ONW or ONTs, producing the laydown and entanglement of the flexible nanostructures, which produced a significant decrease in the resistivity of the sensor. Moreover, as expected for a semiconductor, a temperature-dependent resistance was observed. However, the reduction of the resistivity observed at 100 ºC is much higher than expected, considering the bulk resistivity at this temperature, especially for the ONTs case, indicating a decrease in the contact resistance between the wires induced by the temperature.

The response to oxygen is negligible at room temperature. However, against the expectations, the response is clear at higher temperatures (50 and 100 ºC), which should be barely noticeable even at 100ºC, as reported by other authors, due to the slow diffusion of the gases in crystalline H_2Pc thin films.[67,69] Thus, this effect can be attributed to the high specific area of these 1D and 3D nanostructures, which effectively enhances the oxygen doping of the organic nanostructures. Moreover, the enhancement in the oxygen response by light illumination was quite significant. For the three temperatures studied, the effect of the illumination on the conductivity was independent of the temperature of the samples. This result indicates that the sensors can work at room temperature under illumination, opening a new way for low-cost and long-lasting devices since room temperature operation usually preserves the sensor performance of organic materials.

Therefore, additional experiments with more feasible light sources, such as low-power LEDs, were performed. The spectral dependency on the illumination was tested with three different wavelengths (blue, green and red), showing a similar response even when the red LED overlapped with the absorption band of the H_2Pc molecule. In any case, the enhanced conductivity induced by a low-power LED light can be used to switch ON and OFF the sensor response even at RT. Additionally, this type of device has a high potential for low-power electronics since the sensor is at room temperature (no heating is necessary), which

allows it to work under non-constant operation. This latter aspect will permit an intermittent operation of the sensor, switching ON for some seconds under LED illumination to sense the concentration of a particular analyte.

The promising sensitivity enhancements achieved with metal-free phthalocyanine, facilitated by nanostructuration and photoenhanced effects, suggest that incorporating metallated phthalocyanines or porphyrins could further improve selectivity toward specific analytes. These precursors are also compatible with the direct synthesis methodology for organic nanowires and nanotrees on preformed interdigitated electrodes thus paving the way for future sensors devices with his selectivity, sensitivty and reponse times, that can detect a wider range of oxidative gases. It is important to mention that the nanotree architecture also allows combining different molecules to form the primary and secondary nanowires, which might provide a successful approach to fabricating 1D multi-sensors.

Author contributions

A. Borrás, A. Barranco, J. R. Sanchez-Valencia: conceptualisation. A. Borrás, and A. Barranco: funding acquisition. A. Borrás, J. R. Sanchez-Valencia: writing the original draft. A.N. Filippin, A. Campos-Lendinez, J. Delgado-Alvarez, G. Moreno-Martinez, samples fabrication and sensor assembly. A.N. Filippin, A. Campos-Lendinez, J. Castillo-Seoane, V.J. Rico, V. F. Godinho, and J.R. Sanchez-Valencia performed the sensor characterisation. All the authors were involved in the article's investigation, methodology, validation, review, and editing.

Conflicts of interest

There are no conflicts to declare.

Data availability

The data supporting this article have been included as part of the Supplementary Information.

Acknowledgements

References

1   Y. Xiao, H. Li, C. Wang, S. Pan, J. He, A. Liu, J. Wang, P. Sun, F. Liu and G. Lu, *Advanced Sensor Research*, 2024, **3**, 2300035.

2   N. Goel, K. Kunal, A. Kushwaha and M. Kumar, *Engineering Reports*, 2023, **5**, e12604.

3   Z. Wang, M. Bu, N. Hu and L. Zhao, *Composites Part B: Engineering*, 2023, **248**, 110378.

4   S. Sardana, H. Kaur, B. Arora, D. K. Aswal and A. Mahajan, *ACS Sens.*, 2022, **7**, 312–321.

5   S. Sardana and A. Mahajan, *ACS Appl. Nano Mater.*, 2023, **6**, 469–481.

6   S. Yuvaraja, A. Nawaz, Q. Liu, D. Dubal, S. G. Surya, K. N. Salama and P. Sonar, *Chem. Soc. Rev.*, 2020, **49**, 3423–3460.

7   B. King and B. H. Lessard, *Journal of Materials Chemistry C*, 2024, **12**, 5654–5683.

8   Z. Shen, W. Huang, L. Li, H. Li, J. Huang, J. Cheng and Y. Fu, *Small*, 2023, **19**, 2302406.

9   C. M. Boutry, Y. Kaizawa, B. C. Schroeder, A. Chortos, A. Legrand, Z. Wang, J. Chang, P. Fox and Z. Bao, *Nat Electron*, 2018, **1**, 314–321.

10 J. Polena, D. Afzal, J. H. L. Ngai and Y. Li, *Chemosensors*, 2022, **10**, 12.

11 Y. Huang, X. Fan, S. Chen and N. Zhao, *Adv. Funct. Mater.*, 2019, **29**, 1808509.

12 G. Simone, M. J. Dyson, S. C. J. Meskers, R. A. J. Janssen and G. H. Gelinck, *Adv. Funct. Mater.*, 2020, **30**, 1904205.

13 X. Chen, W. Mao, W. Zhou, P. Huang, H. Liu, X. Wang, Z. Liang, Q. Yang, Y. Chen, G. Zhou and J. Xu, *ACS Appl. Mater. Interfaces*, 2024, **16**, 57512–57523.

14 H. Liu, J. Song, Z. Zhao, S. Zhao, Z. Tian and F. Yan, *Advanced Science*, 2024, **11**, 2305347.

15 J. V. Dcosta, D. Ochoa and S. Sanaur, *Advanced Science*, 2023, **10**, 2302752.

16 W.-D. Li, K. Ke, J. Jia, J.-H. Pu, X. Zhao, R.-Y. Bao, Z.-Y. Liu, L. Bai, K. Zhang, M.-B. Yang and W. Yang, *Small*, 2022, **18**, 2103734.

17 M. Wu, S. Hou, X. Yu and J. Yu, *J. Mater. Chem. C*, 2020, **8**, 13482–13500.

18 H. F. Iqbal, Q. Ai, K. J. Thorley, H. Chen, I. McCulloch, C. Risko, J. E. Anthony and O. D. Jurchescu, *Nat Commun*, 2021, **12**, 2352.

19 J.-H. Kwon, M.-H. Kim and J.-H. Bae, *J. Mater. Chem. C*, 2023, **12**, 29–49.

20 K. Tie, J. Qi, Y. Hu, Y. Fu, S. Sun, Y. Wang, Y. Huang, Z. Wang, L. Yuan, L. Li, D. Wei, X. Chen and W. Hu, *Science Advances*, 2024, **10**, eadn5964.

21 S. Mandal, M. Banerjee, S. Roy, A. Mandal, A. Ghosh, B. Satpati and D. K. Goswami, *ACS Appl. Mater. Interfaces*, 2019, **11**, 4193–4202.

22 H. S. Nalwa, in *Handbook of Surfaces and Interfaces of Materials*, Academic Press, Burlington, 2001, pp. xxv–xxviii.

23 J. Sheng, H.-J. Jeong, K.-L. Han, T. Hong and J.-S. Park, *Journal of Information Display*, 2017, **18**, 159–172.

24 D. Gounden, N. Nombona and W. E. van Zyl, *Coordination Chemistry Reviews*, 2020, **420**, 213359.

25 R. Song, Z. Wang, X. Zhou, L. Huang and L. Chi, *ChemPlusChem*, 2019, **84**, 1222–1234.

26 S. Ganesh Moorthy, J. Arvidson, R. Meunier-Prest, H. Wang and M. Bouvet, *ACS Sens.*, 2024, **9**, 883–894.

27 F. I. Bohrer, A. Sharoni, C. Colesniuc, J. Park, I. K. Schuller, A. C. Kummel and W. C. Trogler, *J. Am. Chem. Soc.*, 2007, **129**, 5640–5646.

28 M. M. El-Nahass, A. M. Farid, A. A. Attia and H. A. M. Ali, *Applied Surface Science*, 2006, **252**, 7553–7561.

29 R. Saini, A. Mahajan, R. K. Bedi, D. K. Aswal and A. K. Debnath, *RSC Advances*, 2014, **4**, 15945–15951.

30 A. E. Pochtennyi and V. K. Dolgiy, *Nanoscience and Technology: An International Journal*, DOI:10.1615/NanoSciTechnolIntJ.2020032278.

31 S. Kumar, A. K. Sharma, M. K. Sohal, D. P. Sharma, A. K. Debnath, D. K. Aswal and A. Mahajan, *Sensors and Actuators B: Chemical*, 2021, **327**, 128925.

32 J. D. Wright, *Progress in Surface Science*, 1989, **31**, 1–60.

33 R. D. Gould, *Coordination Chemistry Reviews*, 1996, **156**, 237–274.

34 A. A. El-Saady, N. Roushdy, A. A. M. Farag, M. M. El-Nahass and D. M. Abdel Basset, *Opt Quant Electron*, 2023, **55**, 662.

35 P. Powroźnik, B. Solecka, P. Pander, W. Jakubik, F. B. Dias and M. Krzywiecki, *Sensors (Basel)*, 2022, **22**, 9947.

36 J. P. Contour, P. Lenfant and A. K. Vijh, *Journal of Catalysis*, 1973, **29**, 8–14.

37 S. Y. Flores, J. Gonzalez-Espiet, J. Cintrón, N. D. J. Villanueva, F. E. Camino, K. Kisslinger, D. M. P. Cruz, R. D. Rivera and L. F. Fonseca, *ACS Appl. Nano Mater.*, 2022, **5**, 4688–4699.

38 Z.-L. Gong, Y. Guo and Y.-W. Zhong, *Mater. Chem. Front.*, 2023, **7**, 6281–6304.

39 A. Kumar, R. Meunier-Prest and M. Bouvet, *Sensors*, 2020, **20**, 4700.

40 D. Klyamer, R. Shutilov and T. Basova, *Sensors*, 2022, **22**, 895.

Nanoscale Accepted Manuscript

41 L. Xiao, S. Yu, Q. Cui, J. Liu, G. Liang, Y. Li and G.-J. Zhang, *Sensors and Actuators B: Chemical*, 2024, **406**, 135402.

42 P. Feng, F. Shao, Y. Shi and Q. Wan, *Sensors*, 2014, **14**, 17406–17429.

43 T. Shaymurat, Q. Tang, Y. Tong, L. Dong and Y. Liu, *Advanced Materials*, 2013, **25**, 2376–2376.

44 M. Sangchap, H. Hashtroudi, T. Thathsara, C. J. Harrison, P. Kingshott, A. E. Kandjani, A. Trinchi and M. Shafiei, *International Journal of Hydrogen Energy*, 2024, **50**, 1443–1457.

45 J. Ding, Z. Zheng, Z. Song, S. Ding, J. Wen, K. Liu, C. Zhang and H. Li, *Materials & Design*, 2023, **234**, 112360.

46 A. Borras, M. Aguirre, O. Groening, C. Lopez-Cartes and P. Groening, *Chem. Mater.*, 2008, **20**, 7371–7373.

47 A. Borras, O. Gröning, M. Aguirre, F. Gramm and P. Gröning, *Langmuir*, 2010, **26**, 5763–5771.

48 M. Alcaire, J. R. Sanchez-Valencia, F. J. Aparicio, Z. Saghi, J. C. Gonzalez-Gonzalez, A. Barranco, Y. O. Zian, A. R. Gonzalez-Elipe, P. Midgley, J. P. Espinos, P. Groening and A. Borras, *Nanoscale*, 2011, **3**, 4554.

49 A. Borras, P. Gröning, J. R. Sanchez-Valencia, A. Barranco, J. P. Espinos and A. R. Gonzalez-Elipe, *Langmuir*, 2010, **26**, 1487–1492.

50 J. Castillo-Seoane, J. Gil-Rostra, V. López-Flores, G. Lozano, F. J. Ferrer, J. P. Espinós, K. (Ken) Ostrikov, F. Yubero, A. R. González-Elipe, Á. Barranco, J. R. Sánchez-Valencia and A. Borrás, *Nanoscale*, 2021, **13**, 13882–13895.

51 M. Macias-Montero, A. N. Filippin, Z. Saghi, F. J. Aparicio, A. Barranco, J. P. Espinos, F. Frutos, A. R. Gonzalez-Elipe and A. Borras, *Advanced Functional Materials*, 2013, **23**, 5981–5989.

52 A. N. Filippin, J. R. Sanchez-Valencia, X. Garcia-Casas, V. Lopez-Flores, M. Macias-Montero, F. Frutos, A. Barranco and A. Borras, *Nano Energy*, 2019, **58**, 476–483.

53 A. N. Filippin, M. Macias-Montero, Z. Saghi, J. Idígoras, P. Burdet, J. R. Sanchez-Valencia, A. Barranco, P. A. Migdley, J. A. Anta and A. Borras, *Scientific Reports*, 2017, **7**, 9621.

54 A. N. Filippin, V. López-Flores, T. C. Rojas, Z. Saghi, V. J. Rico, J. R. Sanchez-Valencia, J. P. Espinós, A. Zitolo, M. Viret, P. A. Midgley, A. Barranco and A. Borras, *Chemistry of Materials*, 2018, **30**, 879–887.

55 A. Nicolas Filippin, J. R. Sanchez-Valencia, J. Idígoras, T. C. Rojas, A. Barranco, J. A. Anta and A. Borras, *Nanoscale*, 2017, **9**, 8133–8141.

56 N. Filippin, J. Castillo-Seoane, M. C. López-Santos, C. T. Rojas, K. Ostrikov, A. Barranco, J. R. Sanchez-Valencia and A. Borrás, *ACS Appl. Mater. Interfaces*, 2020, **12**, 50721–50733.

57 J. Castillo-Seoane, L. Contreras-Bernal, T. C. Rojas, J. P. Espinós, A.-F. Castro-Méndez, J.-P. Correa-Baena, A. Barranco, J. R. Sanchez-Valencia and A. Borras, *Advanced Functional Materials*, **n/a**, 2403763.

58 F.-X. Wang, Y.-Q. Liu, H.-D. Wu, Y. Xiao and G.-B. Pan, *J. Mater. Chem. C*, 2012, **1**, 422–425.

59 Y. Alfredsson, B. Brena, K. Nilson, J. Åhlund, L. Kjeldgaard, M. Nyberg, Y. Luo, N. Mårtensson, A. Sandell, C. Puglia and H. Siegbahn, *The Journal of Chemical Physics*, 2005, **122**, 214723.

60 K. Nilson, J. Åhlund, M.-N. Shariati, J. Schiessling, P. Palmgren, B. Brena, E. Göthelid, F. Hennies, Y. Huismans, F. Evangelista, P. Rudolf, M. Göthelid, N. Mårtensson and C. Puglia, *The Journal of Chemical Physics*, 2012, **137**, 044708.

61 Y. Kim, S.-K. Kang, N.-C. Oh, H.-D. Lee, S.-M. Lee, J. Park and H. Kim, *ACS Appl. Mater. Interfaces*, 2019, **11**, 38902–38909.

62 T. N. Krauss, E. Barrena, T. Lohmüller, J. P. Spatz and H. Dosch, *Phys. Chem. Chem. Phys.*, 2011, **13**, 5940–5944.

63 M. Alcaire, F. J. Aparicio, J. Obrero, C. López-Santos, F. J. Garcia-Garcia, J. R. Sánchez-Valencia, F. Frutos, K. (Ken) Ostrikov, A. Borrás and A. Barranco, *Advanced Functional Materials*, 2019, **29**, 1903535.

64 L. R. Fleet, J. Stott, B. Villis, S. Din, M. Serri, G. Aeppli, S. Heutz and A. Nathan, *ACS Appl. Mater. Interfaces*, 2017, **9**, 20686–20695.

65 K. Toyota, J. Hasegawa and H. Nakatsuji, *J. Phys. Chem. A*, 1997, **101**, 446–451.

66 Y. Ishida, J. K. Jung, M. S. Kim, J. Kwon, Y. S. Kim, D. Chung, I. Song, C. Kim, T. Otsu and Y. Kobayashi, *Commun Phys*, 2020, **3**, 1–8.

67 E. van Faassen and H. Kerp, *Sensors and Actuators B: Chemical*, 2003, **88**, 329–333.

68 D. Tomecek, M. Hruska, P. Fitl, J. Vlcek, E. Maresova, S. Havlova, L. Patrone and M. Vrnata, *ACS Sens.*, 2018, **3**, 2558–2565.

69 K. Kudo, T. Sumimoto, K. Hiraga, S. Kuniyoshi and K. Tanaka, *Jpn. J. Appl. Phys.*, 1997, **36**, 6994.

70 G. A. Kumar, J. Thomas, N. George, N. V. Unnikrishnan, P. Radhakrishnan, V. P. N. Nampoori and C. P. G. Vallabhan, *Journal of Materials Science*, 2000, **35**, 2539–2542.

Data availability

The authors confirm that the data supporting the findings of this study are available within the article and its supplementary materials.

Nanoscale Accepted Manuscript